The role of zonal flows and predator-prey oscillations in triggering the formation of edge and core transport barriers

L. Schmitz,[1] L. Zeng,[1] T.L. Rhodes,[1] J.C. Hillesheim[2] W.A. Peebles,[1] R.J. Groebner,[3] K.H. Burrell,[3] G.R. McKee,[4] Z. Yan,[4] G.R. Tynan,[5] P.H. Diamond,[5] J.A. Boedo,[5] E.J. Doyle,[1] B.A. Grierson,[6] C. Chrystal,[5] M.E. Austin,[7] W.M. Solomon,[6] and G. Wang[1]

[1]University of California Los Angeles, Los Angeles, California 90095-7799, USA

[2]EURATOM/CCFE Fusion Association, Abingdon, Oxon OX14 3DB, UK

[3]General Atomics, PO Box 85608, San Diego, California 92186-5608, USA

[4]University of Wisconsin-Madison, Madison, Wisconsin 53706, USA

[5]University of California San Diego, 9500 Gilman Dr., La Jolla, California 92093-0417, USA

[6]Princeton Plasma Physics Laboratory, Princeton, New Jersey 08543-0451, USA

[7]University of Texas-Austin, Austin, Texas 78712, USA

Corresponding author: lschmitz@ucla.edu

Abstract. We present direct evidence of low frequency, radially sheared, turbulence-driven flows [zonal flows (ZFs)] triggering edge transport barrier formation preceding the L- to H-mode transition via periodic turbulence suppression in limit-cycle oscillations (LCO), consistent with predator-prey dynamics. The final transition to ELM-free H-mode occurs after the equilibrium $E \times B$ flow shear increases due to ion pressure profile evolution. Zonal flows are also observed to initiate formation of an electron internal transport barrier (ITB) at the $q = 2$ rational surface via local suppression of electron-scale

turbulence. Multi-channel Doppler Backscattering (DBS) has revealed the radial structure of the ZF-induced shear layer and the $\boldsymbol{E} \times \boldsymbol{B}$ shearing rate, $\omega_{E \times B}$, in both barrier types. During edge barrier formation, the shearing rate lags the turbulence envelope during the LCO by 90º, transitioning to anti-correlation (180º) when the equilibrium shear dominates the turbulence-driven flow shear due to the increasing edge pressure gradient. The time-dependent flow shear and the turbulence envelope are anti-correlated (180º out of phase) in the electron ITB. Limit cycle oscillations with time-reversed evolution dynamics (transitioning from an equilibrium-flow dominated to a ZF-dominated state) have also been observed during the H-L back-transition and are potentially of interest for controlled ramp-down of the plasma stored energy and pressure (normalized to the poloidal magnetic field) $\beta_\theta = 2\mu_0 n \left(T_e + T_i\right) \big/ B_\theta^2$ in ITER.

PACS No.:   52.35.Ra, 52.25.Fi, 52.55.Fa, 52.70.Gw

1. Introduction

High confinement-mode (H-mode) operation is almost certainly required in future burning plasma experiments to achieve economical fusion energy production. Access to H-mode requires sufficient auxiliary heating power, and is challenging in large fusion plasmas where neutral beams at very high energy would be required to heat the core plasma. The 2008 International Tokamak Physics Activity (ITPA) scaling law for the L-H transition power threshold, P_{th} (MW) = 0.049 $B_\Phi^{0.8}$ $n_e^{0.72}$ $S^{0.94}$ [1], is derived from an international, multi-machine database. This scaling reflects only the dependence of the L-H transition power threshold on plasma density n_e $\left(10^{20}\ \mathrm{m}^{-3}\right)$, toroidal magnetic field B_ϕ (T), and the plasma surface area S $\left(\mathrm{m}^2\right)$. However, the threshold power has been shown to depend on additional parameters such as isotopic plasma composition, plasma shape, divertor geometry, and the beam-induced and intrinsic torque [2–5]. A physics-based model of the L-H transition threshold power is therefore needed to confidently extrapolate to auxiliary heating requirements for ITER and future burning plasma experiments. Understanding the trigger event or mechanism leading to localized turbulence reduction or suppression near the magnetic separatrix (and initiating formation of a highly localized edge transport barrier), as well as the spatio-temporal evolution of the edge transport barrier, are important steps in developing such a physics-based transition model.

Analogous to edge barriers, internal transport barriers (ITBs) can form spontaneously with sufficient auxiliary heating (or α-particle heating in burning plasmas), and their

presence directly affects core plasma temperature and thermal confinement, as well as the ratio of electron-to-ion temperature and fusion yield. At low or moderate neutral beam or radiofrequency heating power at reversed magnetic shear, internal barriers are often triggered at the radii where low order rational magnetic surfaces enter the plasma [6–8]. This has been attributed to stationary zonal flows (ZFs) near the rational surfaces (in particular the $q = 2$ surface [8–10]). At higher heating power, the formation radius of transport barriers does not necessarily coincide with the location of rational magnetic surfaces.

After the realization that sufficiently large $E \times B$ flow shear can substantially reduce the local turbulence and radial transport level [11], experiments have demonstrated that sheared flow indeed plays a crucial role in triggering edge and core barrier formation, and in maintaining turbulence suppression in the H-mode pedestal and in sustained internal barriers (for example, [7,8,10–17]). With neutral beam injection and driven ion rotation v_i, barriers can be supported via sheared $E \times B$ rotation resulting from the $v_i \times B$ term in the radial momentum balance, or due to the ion pressure gradient, depending on the plasma regime, barrier evolution, and other experimental details. The trigger mechanism initiating $E \times B$ shear and turbulence suppression during barrier formation has not been conclusively identified for either edge or internal core barriers, although recent experimental evidence [18–24] and theoretical modeling [25,26] point strongly towards turbulence-generated $E \times B$ flows (or ZFs) as the critical element. The energy transfer from the turbulence spectrum into low frequency turbulence-driven flows, via the nonlinear Reynolds stress, has been directly measured recently during edge barrier formation, supporting this physical picture [27,28].

In this paper we examine the trigger physics of both edge and internal transport barriers, using novel diagnostic capabilities to simultaneously map the evolution of plasma $E \times B$ flow and turbulence amplitude with high spatial and temporal resolution. Section 2 discusses low frequency limit cycle oscillations (LCOs) triggering turbulence suppression at transport-relevant poloidal wavenumbers [$0.3 \leq k_\theta \rho_s \leq 0.6$, where k_θ is the poloidal turbulence wavenumber and $\rho_s = c_s M_i / eB$ is the ion sound gyroradius, with $c_s = \left(k T_e / M_i \right)^{1/2}$, the Boltzmann constant k_B, the electron temperature T_e, and the ion mass M_i], and initiating the L- to H-mode transition near the power threshold. For heating power above the threshold, rapid transitions executing only a partial limit cycle are observed. In both cases, increasing equilibrium $E \times B$ shear locks in the final transition to H-mode confinement as the ion pressure gradient increases (either gradually or rapidly) due to (locally) reduced radial particle and heat flux. Limit cycle oscillations between the local turbulence amplitude and $E \times B$ flow/flow shear have also been observed during the H-L back-transition; initial results are presented and discussed in section 3. Measurements of localized low frequency ZF structures, suppressing electron-scale turbulence $\left(k_\theta \rho_s \sim 2 \right)$ and initiating formation of an electron ITB at the $q = 2$ rational surface, are discussed in section 4. Finally, a summary and comparison of the observed ZF characteristics and trigger dynamics in edge and core transport barriers is given in section 5.

2. Predator-prey limit cycle triggering the L-H transition

Evidence of turbulence-generated shear flows preceding the L-H transition has been recently found in several experiments [18–24,25]. In most of these experiments, periodic

or intermittent low frequency shear flows (<5 kHz) were investigated, however intermittent ZFs at the Geodesic Acoustic Mode (GAM) frequency have also been documented [19]. In DIII-D, edge turbulence properties and edge barrier formation have been studied at and above the L-H transition power threshold (>1 MW neutral beam co-injection into a lower single-null (LSN) diverted L-mode plasma with line-averaged density $\langle n_e \rangle \sim 2.5 \times 10^{13}$ cm^{-3}, $B_\phi = 2$ T, and plasma current $I_p = 1.1$ MA). We report here detailed, radially resolved measurements of turbulence and shear flow evolution, during L-H transitions with neutral beam heating power close to L-H transition power threshold, and significantly above threshold. Experimental evidence for limit cycle oscillations between the $E \times B$ velocity and the density fluctuation envelope $\tilde{n}$ inside the last closed flux surface (LCFS) have been clearly observed [22].

The turbulence and flow measurements reported here employ multi-channel microwave Doppler backscattering (DBS) [29–31] which on DIII-D utilizes multi-frequency, co-linear diagnostic microwave beams launched at an oblique angle to the magnetic flux surfaces (in the plane perpendicular to the magnetic field B). Backscattering by plasma density fluctuations occurs preferentially near the cutoff layer [30], according to the selection rules $k_s = -k_I = 2k_\theta$ and $\omega_s = \omega_I + v_t k_\theta$, where the indices I and s denote the incident and backscattered wave, v_t is the poloidal turbulence advection velocity, and k_θ is the resonant poloidal density fluctuation wavenumber. The backscattered signal amplitude is proportional to the density fluctuation amplitude $\tilde{n}(k_\theta)$. The probed wavenumber k_θ and the probed major radius R are obtained using GENRAY ray tracing [32]. The time-resolved $E \times B$ velocity is obtained from the instantaneous Doppler shift, $f_D = (\omega_s - \omega_L)/2\pi = v_t k_\theta/(2\pi)$, with $v_t = v_{E \times B} + v_{ph}$ [33].

Neglecting the (typically small) contribution of the fluctuation phase velocity v_{ph}, one obtains $v_{E\times B} \approx 2\pi\, f_D/k_\theta$. An attempt was made to place an upper limit on the poloidal turbulence phase velocity by evaluating the turbulence advection velocity in successive shots where the DBS system was probing different poloidal wavenumbers. The differences in measured advection velocity were within the standard deviation, suggesting that the phase velocity is $\leq\pm15\%$ of the measured advection velocity in L-mode, and in the LCO and H-mode phases.

Figure 1 shows the time evolution of the divertor D_α light emission, the turbulence level (at $k_\theta \rho_s \sim 0.45$), the line-averaged plasma density, and the local electron temperature (at major radius $R = 2.23$ m, $\sim 4\pm0.5$ cm inside the LCFS), in a lower single-null (LSN), low triangularity diverted plasma with neutral beam co-injection. The neutral beam power is stepped from 0 to 1.1 MW (close to the L-H transition power threshold in this plasma) at 1010 ms, leading to an oscillation in the $E \times B$ velocity just inside the last closed flux surface after 1105 ms [figure 1(d,e)], and a simultaneous fast reduction (and consecutive periodic oscillation) in the edge density fluctuation level $\tilde{n}$ [shown in figure 1(b) is $\tilde{n}$ at 2.25 m]. The divertor D_α emission decreases periodically, indicating a modulation of the particle flux across the LCFS. The $E \times B$ velocity oscillation initially decreases in frequency [figure 1(d)] and then remains constant at about 1.5 kHz. The neutral beam power is stepped up to 2.2 MW at 1250 ms. Following this power step, the oscillation frequency of $\tilde{n}$ and $v_{E\times B}$ gradually decreases, while the $E \times B$ velocity fluctuation amplitude increases substantially. After 1338 ms, the final transition to H-mode occurs (indicated by a low residual D_α signal level with isolated D_α emission events which have been identified as type III edge-localized modes (ELMs), via a typical

ELM precursor which is present in the Mirnov loop magnetic signals). The line-averaged plasma density and the edge electron temperature increase gradually during the extended oscillation period and after the H-mode transition [figure 1(c)].

The observed edge plasma $E \times B$ flow oscillation has been shown to be consistent with a LCO between the turbulence intensity and a turbulence-driven flow [22]. It has been shown that the LCO has the characteristics of a ZF predator-prey oscillation characterized by toroidal/poloidal symmetry ($n_\phi = 0$ $n\phi = 0$, $m_\theta = 0$, $m\theta = 0$ where n_ϕ and m_ϕ are the toroidal and poloial mode number, respectively), a finite radial wavenumber ($k_r \sim 0.7$ cm^{-1}), and a 90º phase lag of the ZF with respect to the density fluctuation envelope $\tilde{n}/n$.

Figure 2(a) shows a time evolution contour plot of the $E \times B$ velocity across and inside the LCFS in a different plasma shot (#140426), as determined via multi-channel DBS from turbulence poloidal advection [30,33]. In this shot the plasma shape is identical to the shot shown in figure 1, however the neutral beam power is initially at 0.85 MW, and is increased at $t = 1240$ ms to 4.2 MW (preceding the time window shown in figure 2). This power level is substantially above the L-H transition power threshold. Accordingly, limit cycle oscillations are present during a shorter time period (~16 ms) before the final transition to H-mode occurs. Twelve radii are probed simultaneously by the Doppler backscattering system. The DBS probing locations (X-mode cut-off layer) were mapped to a radial grid for this data set via GENRAY ray tracing [32], based on high time resolution (25 µs) electron density profiles from profile reflectometry. The LCFS location is determined within ±0.5 cm uncertainty from EFIT magnetic equilibrium reconstruction, cross-checked in discharges in the same plasma shape by reciprocating

probe data (using the floating potential drop as indicator of the transition to the closed field line region). When the LCO starts at 1271.7 ms, the $\boldsymbol{E} \times \boldsymbol{B}$ velocity periodically becomes negative at and just inside the LCFS. The negative flow increases with time and the flow layer widens radially and expands radially inwards, increasing in width from ~2 cm after the start of the LCO. Around 1288 ms, the transition to ELM-free H-mode takes place after a final transient, characterized by a radially extended flow layer ~3–3.5 cm in width, with flows reaching ~ -6 km/s after the transition to H-mode. The LCFS moves slightly inwards (by less than 0.5 cm) after the H-mode transition. Figure 2(b) shows that the normalized density fluctuation level $\tilde{n}/n$ (proportional to the amplitude of the scattered DBS signal) is periodically reduced during the LCO [the probed poloidal wavenumber is $k_\theta \rho_s \sim 0.45$ with $\Delta k_\theta / k_\theta \sim 0.3$, consistent with the wavenumber range characteristic of ion temperature gradient (ITG), trapped electron modes (TEMs), and/or resistive ballooning modes (RBMs)]. As described above, our measurements did not allow determination of the direction or magnitude of the turbulence phase velocity, hence the dominant turbulence mode could not be definitively identified. Sustained turbulence reduction is observed at the H-mode transition at $t_H \sim 1288$ ms [figure 2(b)]. The periodic decrease in the D_α recycling light [figure 2(c)] indicates modulation of the radial particle outflow past the LCFS due to periodically reduced local radial particle transport.

The limit cycle between $\tilde{n}/n$ and $v_{E \times B}$, 3 cm inside the LCFS, is shown in figure 2(d). It is important to note that the $\boldsymbol{E} \times \boldsymbol{B}$ flow shown here contains a positive contribution due to neutral beam injection (NBI) driven plasma co-rotation [estimated from carbon charge exchange recombination (CER) data as ~ 3–4 km/s] and a smaller

(negative) contribution due to the L-mode ion pressure gradient (estimated as ~ -1 km/s at this radius from profile reflectometry and CER carbon ion temperature data), in addition to the (oscillating) turbulence-driven (ZF) flow. Hence, at the location investigated here, a less positive E_r corresponds to a deeper edge electric field well. The $\boldsymbol{E} \times \boldsymbol{B}$ flow oscillation lags $\tilde{n}/n$ by 90º (data points are taken during a 0.8 ms time interval starting at $t = 1272.5$ ms during the LCO, ~3 cm inside the LCFS). The initial limit cycle dynamics can be thought of as a predator-prey relationship between the $\boldsymbol{E} \times \boldsymbol{B}$ flow generated from the turbulence via the nonlinear Reynolds stress, and the energy density in the turbulence [27,28]. As the turbulence level grows with increasing neutral beam heating power in L-mode, turbulence-driven flows are eventually triggered at and just inside the separatrix where the fluctuation level and energy density are highest. The flow shear associated with the ZF then reduces the turbulence saturation level. In the data shown in figure 2(d) this phase corresponds to the lower right corner of the limit cycle. In turn, the ZF cannot be sustained due to the decreasing turbulence level and the $\boldsymbol{E} \times \boldsymbol{B}$ velocity increases (lower left corner of the limit cycle). Once the ZF shear becomes too small to maintain turbulence quench, the turbulence level driven by the radial temperature and/or pressure gradients grows while $v_{E \times B}$ becomes more positive. The turbulence level finally increases again to the point where ZFs are triggered, and the cycle repeats.

We have previously shown [22] that $\boldsymbol{E} \times \boldsymbol{B}$ flow shear due to the gradually increasing ion pressure gradient increases during the LCO, as edge confinement improves. This diamagnetic component of the total $\boldsymbol{E} \times \boldsymbol{B}$ shear is also called equilibrium flow shear here, although one has to keep in mind that the ion pressure gradient can be modulated during the LCO as a result of the modulation in the local transport coefficients as the

turbulence level changes, and hence the diamagnetic flow component may have a modulated or oscillatory component also. Our previous measurements show that the diamagnetic contribution to E_r becomes dominant well after the start of LCO [22]. As the LCO progresses, radial transport is reduced during each LCO cycle, leading to a periodic modulation of the pressure gradient and $E \times B$ profile shear. In addition, the average pressure gradient has been found to increase gradually. The diamagnetic contribution to E_r and the corresponding $E \times B$ shear become dominant during the LCO after the ZF collapses during each predator-prey cycle, delaying the turbulence recovery further within each successive limit cycle. This increasing delay slows down the limit cycle frequency, as seen in figures 1(d) and 2(a). Figure 1(e) also shows that the amplitude of the $E \times B$ velocity oscillation increases with time, first gradually and then very substantially towards the final H-mode transition. This indicates either that the energy transferred from the turbulence to the turbulence-generated flow increases before the final transition to H-mode, or that the equilibrium flow due to pressure gradient evolution increases at this time. Both of these observations (frequency reduction and flow increase) are qualitatively consistent with the two-predator, one prey model advanced presently [26], where both the turbulence-driven flow (predator 1) and the equilibrium flow and flow shear (predator 2) increase over time, but the equilibrium flow shear becomes dominant just before the transition to sustained H-mode.

A similar conclusion regarding the increasing influence of pressure-gradient driven flow and flow shear during the LCO has been reported from the HL-2A tokamak [23]. In this experiment two types of limit cycles were observed, with the interaction between the density profile modulation and the radial electric field dominant before the final H-mode

11

transition. In contrast to the results reported here, in a recent experiment in JFT-2M [34], evidence for limit cycles involving the turbulence level, the density gradient, and radial electric field was found, and it was concluded that turbulence-driven flow was not important for the observed LCO dynamics. An experiment in the TXTOR tokamak, where a positive edge electric field was generated via electrode biasing showed strong evidence of LCO only involving turbulence-driven flow [34]. The detailed radial structure of the limit cycle and its dependence on plasma parameters is presently still investigated in DIII-D and elsewhere.

Figure 3 shows the time evolution of the $E \times B$ velocity and the normalized density fluctuation level across the transition, from L-mode to the LCO, and to the final H-mode state, at three radii near the separatrix ($R = 2.27$ m), near the center of the well in the radial electric field ($R = 2.25$ m), and inboard of the electric field well ($R = 2.225$ m). It is clear that the $E \times B$ velocity oscillates and becomes progressively more negative at the separatrix and 2 cm inside the separatrix during the LCO, while the fluctuation level is periodically reduced [the phase shift between $v_{E \times B}$ and $\tilde{n}$ is initially 90º as shown in figure 2(d)]. Figure 3(a) also shows the increasing $E \times B$ velocity inboard of the electric field minimum ($R = 2.225$ m). The associated flow shear hence increases both in the outboard and inboard shear layer. After the final H-mode transition at $t \sim 1286$ ms, strong negative $E \times B$ flow is sustained at $R = 2.27$ m and 2.25 m (there is an isolated type-III ELM temporarily reducing the electric field/shear at 1288 ms). The $E \times B$ flow at 2.225 m becomes negative at $t \sim 1291$ ms, as the electric field well expands radially with the inboard shear layer moving further inwards [as seen in figure 2(a)].

12

Figure 4 shows radial profiles of the normalized density fluctuation level, plasma density, and $E \times B$ velocity in L-mode (before start of the LCO, and in H-mode, for the experimental conditions discussed above). Normalized fluctuation levels in H-mode are reduced by about a factor of ~1.5 compared to L-mode at the separatrix, but by a larger factor further inwards within the electric field layer. It is apparent that the electric field layer widens considerably in H-mode, and that the inboard shear layer contributes substantially to fluctuation suppression. The density profile steepens throughout the electric field layer, but most prominently at the outer/inner shear layer radii (the profiles have been obtained via averaging eight reflectometry profiles over 0.4 ms; the density measurement standard deviation is roughly 9%). The radial localization of the DBS channels is determined via ray tracing, based on profile reflectometry data also, hence the radial alignment error of the fluctuation and flow velocity profiles is relatively small (± 0.25–0.4 cm, given by the standard deviation of the density profile measurement as indicated).

In the presence of radially sheared flow, characteristic changes in the turbulent eddy topology are expected [11,34], in particular poloidal elongation and stretching reflected in an increased poloidal correlation length, and a simultaneous decrease in the radial correlation length. The radial turbulence correlation length λ_r has been determined from five closely spaced DBS channels probing a radial range approximately 1 cm in width (with an inter-channel spacing $\Delta r \approx 0.25$ cm). During time periods when turbulence is reduced in the LCO, the radial correlation length is reduced by about 30% [figure 5(a,b), which shows the auto-correlation and radial cross-correlation coefficients of the back-scattered DBS signal]. In H-mode, λ_r is further reduced by 40% compared to the LCO

time periods with reduced turbulence. In figure 5(b,c), the data from the DBS channel separated by 0.75 cm from the reference channel is not statistically significant and has been omitted. The DBS diagnostic cannot presently provide a measurement of poloidal turbulence correlation length. However, highly anisotropic eddies with $\lambda_\theta >> \lambda_r$ have been observed via beam emission spectroscopy (BES) at lower poloidal wavenumber ($k_\theta \leq 3\ \mathrm{cm}^{-1}$) with λ_θ increasing from 5 cm in L-mode to 7 cm in H-mode. Both the observed reduction in radial correlation length and the increasing anisotropy/increasing poloidal correlation length support the physical picture of shear stabilization [10,11] in the LCO during the phase of reduced density fluctuation level $\tilde{n}$, and in sustained H-mode.

In a "regular" L-H transition in the same LSN divertor configuration (#140439), but with beam power well above the transition threshold (L-mode density $\langle n \rangle \sim 1.5 \times 10^{19}\ \mathrm{cm}^{-3}$), turbulence-driven, toroidally and poloidally symmetric flows have been documented here as short transients executing only part of one limit cycle period over ~2 ms [figure 2(e), showing two data sets for major radii 3.5–4.5 cm inside the LCFS]. This observation suggests that the turbulence-driven flow and the subsequent increase in equilibrium shear may occur in regular transitions, well above the L-H power threshold, in a similar fashion than in LCO transitions, except that no complete limit cycle is executed as the equilibrium shear increases on the LCO timescale. This observation also suggests that the LCO state may be maintained for a long time period if the auxiliary power is kept very close to the threshold power (as observed previously [19]). Figure 6 shows the corresponding time evolution of density fluctuations [figure 6(a,c)], the total $E \times B$ shearing rate $\omega_{E \times B}$ and turbulence decorrelation rate

$\Delta\omega_D$ [figure 6(b,d)], for two radii 0.5 cm and 2 cm inside the LCFS, and the radial density and ion pressure gradients spanning the two radii (coinciding with the region where the density gradient is largest) [figure 6(e,f)]. The density gradient was evaluated from profile reflectometry data. The main ion pressure gradient was approximated using density profiles from profile reflectometry, and the carbon ion temperature from CER. Main ion dilution is neglected here as $Z_{eff} < 1.6$. Just inside the LCFS, the density fluctuation level decreases as the flow shearing rate exceeds the decorrelation rate [figure 6(a,b)]. A brief flow oscillation corresponding to a partial LCO cycle [figure 2(e)] is evident. Radial transport begins to decrease as reflected by the reduced D_α signal [figure 6(f)]. Further inboard (about 2 cm inside the LCFS), the flow shearing rate increases with a delay of 0.6–0.7 ms compared to the outboard location, again suppressing fluctuations once $\omega_{E\times B} > \Delta\omega_D$ [figure 6(c,d)]. The radial density gradient increases mainly after fluctuations have been suppressed/reduced across the edge layer, and the further increase in $\omega_{E\times B}$ after 1294 ms can be ascribed to the increasing diamagnetic flow contribution, as the density (pressure) gradient steepens after the initial fluctuation suppression.

Hence the "regular" transition exhibits a similar phenomenology, on a condensed time scale, as the extended LCO transitions discussed earlier. Turbulence suppression due to ZF shearing is first observed in both transition types near the separatrix when the turbulence decorrelation rate $\Delta\omega_D$ decreases sharply concomitantly with an increasing $E \times B$ shearing rate $\omega_{E\times B}$ due to ZF onset. We conjecture that the LCO is always present, however for heating power much above the L-H power threshold, L-H transitions occur on a timescale as short as 100 μs, considerably faster than the transition shown in

figure 6. This is short compared to the characteristic LCO period, and the transition from turbulence-driven flow shear to dominant profile shear occurs within a fraction of an LCO cycle. Conversely, very close to the L-mode-LCO power threshold, the LCO could likely be maintained for very long time intervals (limited only by the discharge duration), as was shown for a limit cycle oscillation with embedded Geodesic Acoustic Modes (GAMs) [19].

Additional strong experimental evidence for the two-predator, one-prey model comes from the time evolution of the phase shift between $\tilde{n}/n$ and the shearing rate $\omega_{E\times B}$ (figure 7). Before the LCO starts, no significant correlation between the two quantities is found [$t_0 - 2.5$ ms in figure 7(a)]. Early during the LCO [$t_0 + 1$ ms in figure 7(a)] and at the start of the regular "fast" transition ($t = 1294.63$ ms), $\omega_{E\times B}$ lags $\tilde{n}/n$ by roughly 90º, consistent with a predator-prey cycle between $\tilde{n}/n$ and $\omega_{E\times B}$. Later during the LCO, just before steady (ELM-free) H-mode confinement is realized, the phase shift increases to 180º in both the extended LCO [$t_0 + 2.5$ ms, figure 7(a)] and in the "regular" transition [1296.03 ms, figure 7(b)]. A phase shift near 180º represents a strong indication that equilibrium shear is dominating the oscillatory ZF shear. The recently developed predator-prey model (extended to include 1-D radial profiles and radial transport) also reflects this change in phase shift [26].

3. Limit cycle oscillations during the H-L back-transition

Limit cycle oscillations were also recently observed during the H-L back-transition (figure 8), showing similar predator-prey characteristics and behavior complementary to the forward transition. The H-L back transition and in particular the H-LCO-L back-transition sequence are important for investigating the interaction between core and edge

16

turbulence, and to directly measure potential turbulence spreading from the top [35]. Figure 8 shows first an H-LCO back transition where the limit cycle frequency [figure 8(c)] increases with time (reflecting a diminishing influence of the equilibrium shear) and the flow amplitude decreases with time, eventually leading to the LCO-L back-transition. Well into the LCO period $\omega_{E \times B}$ lags $\tilde{n}/n$ by 90º as seen in the forward transition discussed earlier. Hence the forward transition sequence is reversed, while the 90º phase lag of $\omega_{E \times B}$ with respect to $\tilde{n}$ is preserved. Around 3610 ms, a second forward L-LCO transition occurs, about 100 ms after the neutral beam power has been increased, with the limit cycle frequency showing the characteristic slow-down, then transitioning to steady ELM-free H-mode around 3960 ms. There is a clear hysteresis in onset neutral beam heating power at the H-LCO and the LCO-L back-transitions compared to the respective forward transitions.

Back-transition LCOs are potentially important for controlled ramp-down of β_θ in ITER, as they may assist in achieving a "soft landing" of the discharge, and may help avoid undue loads on the poloidal field system and power supplies that could result as vertical stability has to be maintained during the ramp-down. It should be noted that the H-LCO back-transition shown in figure 8 is initiated by a Type-I ELM event (visible in the D_α data) that may transiently reduce the equilibrium ion pressure gradient and related equilibrium shear, and thus allow the ZF to grow. The transient increase of the $E \times B$ flow velocity apparent here before the type-I ELM is not typically present in other discharges [figure 8(c)] and does not seem to be related to the back transition trigger. We also note that due to the high spectral frequency resolution chosen here, the time resolution of the velocity spectrum [figure 8(c)] and the integrated velocity [figure 8(d)]

is ~10 ms, so that fast changes of the velocity amplitude and spectrum are artificially broadened and do not exactly track the time resolution of the data shown in figure 8(a,b). Edge magnetic activity was not detected except for a typical precursor oscillation associated with the initial type-I ELM. The maximum negative radial electric field at the H-LCO transition is $E_r \sim$ -18 kV/m, compared to $E_r \sim$ -1.6 kV/m at the LCO-L-mode transition (using the LCO E_r minima). In the forward transition, the corresponding values are $E_r \sim$ -3.35 kV/m at the L-mode-LCO transition, and $E_r \sim$ -12 kV/m at the LCO-H-mode transition. Comparing forward and back-transitions one has to keep in mind however that the ELM preceding the back transition reduces the edge pressure gradient and the radial electric field; after the ELM crash $E_r \sim$ -9 kV/m which is below the value obtained in the forward transition. Hence we find a hysteresis in E_r both for the L-LCO and LCO-H transition. Further research is in progress to identify under which conditions back-transition LCOs can be initiated without ELM trigger, in order to decouple the H-L back-transition dynamics from the ELM evolution.

4. Zonal flows triggering electron ITB formation

With early neutral beam heating in DIII-D, ion and electron internal transport barriers are routinely formed during the current ramp-up as the safety factor reduces and successive rational q-surfaces enter the plasma [8,10]. It has been described earlier in detail how ITBs in reversed shear L-mode plasmas are triggered when the $q = 2$ surface enters the plasma.

Earlier theoretical work has ascribed the trigger to the rarefaction of rational magnetic surfaces around $q = 2$, giving rise to local zero-mean frequency ZF structures [9].

Indications of transient, localized $E \times B$ flows and transiently reduced ion-scale turbulence during ion ITB formation have been previously observed by BES [8,10]. Here we report simultaneous measurements of $E \times B$ velocity and electron-scale density fluctuation amplitude during electron ITB formation.

Figure 9 shows the time evolution of the $E \times B$ flow velocity, the $E \times B$ flow shear (determined from the difference in flow velocity between two neighboring DBS channels), and the density fluctuation amplitude at three radii as an ITB is formed near $r/a = 0.5$ during plasma current ramp in a reversed-shear L-mode plasma (line-averaged density $\langle n \rangle = 2.1 \times 10^{13}$ cm^{-3}, $B_\phi = 2$ T). The radial resolution of each DBS channel is better than 1 cm. The probed poloidal wavenumber is $k_\theta \rho_s \sim 2$ $k_\theta \rho_s \sim 2$ (with a wavenumber resolution $\Delta k_\theta / k_\theta \sim 0.5$). This wavenumber range comprises the upper TEM range –and the lower end of the electron temperature gradient (ETG) range (the linear ETG growth rate peaks however typically at substantially higher wavenumbers $k_\theta \rho_s \sim 5$–10). Motional Stark effect (MSE) polarimetry indicates that $q_{min} = 2$ enters the plasma at 1210–1220 ms, at a radius $r/a \sim 0.5 \pm 0.05$. The shearing rate for $r/a \sim 0.5$ increases within $\sim$200 μs at $t \sim 1212$ ms, and fine-scale radial structure in the $E \times B$ flow begins to evolve near $r/a \sim 0.5$ [figure 9(c)], starting at $t \sim 1207$ ms, just before the $q = 2$ surface enters the plasma. We attribute this drop in $v_{E \times B}$ and the resulting increased radial flow shear to local ZF excitation from the turbulence spectrum in the vicinity of the $q = 2$ surface. Stepwise reductions in the electron-scale density fluctuation level are observed in the two outer DBS chords spanning $0.5 \le r/a \le 0.56$, for 1207 ms $< t < 1224$ ms, concomitantly with large increases in local shear as indicated by dashed vertical lines. A sustained decrease sustained decrease in fluctuation level is

obvious in particular for $r/a = 0.5$. After the $q = 2$ surface enters the plasma, further reduction in q_{min} leads to radial splitting of the $q = 2$ surface. The dip in the shearing rate observed at $t = 1220$ ms is likely a result of the DBS probing location crossing a zone with zero shear in between the two resonant magnetic surfaces. The radial width of the ZF mesoscale radial electric field structure can be estimated at ~2–5 cm from DBS data in the plasmas investigated here, similar to the width of the edge electric field well during the LCO and in H-mode, and corresponding to $k_r \sim 1\text{–}3 \text{ cm}^{-1}$. However, in contrast to the edge barrier, no oscillatory behavior or LCO has been measured in the core barrier. No MHD activity was detected via Mirnov coils during the time period analyzed here.

The time evolution of the radial electron temperature profile, measured via both electron cyclotron emission and Thomson scattering, is shown in figure 10(a). Local steepening of the electron temperature gradient is evident at 1225 ms (about 10 ms after the ITB trigger event), with the electron ITB fully developed after 1270 ms (shown here is data for 1285 ms). The $q = 2$ surface splits eventually as q_{min} reduces further after 1240 ms and a concomitant ion ITB forms after 1260 ms inboard of $r/a = 0.4$ (inside the radius that DBS can probe at this density; shown here for 1271 ms).

A detailed measurement of a quasi-stationary ITB shear layer has been made in a different shot (#133678), where an electron ITB has been maintained for several hundred ms, and the position of the $q = 2$ surface was relatively constant (figure 11). The radial electron temperature profile, and the inverse radial temperature gradient scale length are shown in figure 11(a,b). A DBS system with four closely spaced channels has been used (with channel separation $\Delta r_{ch} \sim 0.5$ cm, as determined by the experimental electron

density gradient). A fine-scale, radial double shear layer with positive outboard and negative inboard $E \times B$ flow shear [$\Delta r \sim$ (4–6) $\rho_s \sim$ 1.5–2 cm, figure 11(c)] is observed at the $q = 2$ surface. The level of electron-scale density fluctuations $\left(k_\theta \rho_s \sim 2\right)$ is reduced in the region of sheared flow [figure 11(d)]. The spatial structure of this shear layer is very similar to the edge barrier shear layer discussed in section 2. The $E \times B$ flow is composed of steady-state and fluctuating (broadband) components with a frequency spectrum $f_d \leq 5$ kHz, reminiscent of edge ZFs observed in DIII-D. In contrast to earlier observations of turbulence suppression in an ion ITBs near $q = 2$ [7], no large-scale barrier is obvious in this experiment in the ion temperature (or density) profile, but the charge exchange recombination/Thomson scattering diagnostic chords are too coarsely spaced to detect possible localized steepening of the ion temperature/pressure profile on the scale of the observed $E \times B$ shear layer. Such a local corrugation in the pressure profile may help sustain the electric field well once turbulence and ZF diminish during barrier formation. From cross-correlation measurements of the instantaneous density fluctuation level and the flow-shearing rate, anti-correlation of shear and density fluctuation amplitude is found (figure 12). This observation is similar to the edge transport barrier discussed in section 2, where anti-correlation is observed once the edge barrier is dominated by equilibrium shear. Figure 13 shows that the correlation coefficient of the density fluctuation level and the $E \times B$ shearing rate in the ITB inboard and outboard shear layer is negative [figure 13(a,c)], while it is close to zero in the embedded shear-free zone [figure 13(b)].

5. Conclusions

In this paper we have presented evidence that both core and edge transport barriers can be triggered via transient low frequency turbulence-generated flows. A similar well structure in the radial electric field (and $E \times B$ velocity) forms in both barrier types, with radial extent $\sim 4-6$ ρ_s in the electron ITB and $\sim 10-20$ ρ_s in the edge barrier, although the radial ZF structure in the ITB can be more complex during initial formation due to the presence of a low order rational magnetic surface. Similarities between both barrier types include a region free of $E \times B$ shear embedded within an outer (positive) and inner (negative) shear layer. The turbulence scale observed here in the edge transport barrier formation is characteristic of turbulence related to ITG/TEM, or RBMs. In contrast, in internal electron thermal barrier formation, reduction of electron-scale turbulence $\left(k_\theta \rho_s \sim 2 \right)$ has been found. The ZF shear layer in the electron ITB forms during q-profile evolution as $q_{min} \sim 2$, roughly at plasma mid radius. Direct evidence for suppression of electron-scale density fluctuations has been found, with a 180º phase shift between fluctuation level and shearing rate. We have shown that the equilibrium pressure gradient eventually increases locally, maintaining the $E \times B$ shear layer after fluctuations subside and the turbulence-driven ZF is damped. In contrast, near the L-H transition power threshold the edge barrier is triggered via extended predator-prey limit cycle oscillations, with an initial phase shift of 90º between $\tilde{n}$ and $\omega_{E \times B}$. Only later during the LCO this phase shift transitions to 180º as equilibrium shear from pressure profile evolution becomes dominant, eventually sustaining turbulence suppression in the transition to steady ELM-free H-mode. Limit cycle oscillations involve oscillatory flow shear driven by the turbulence radial intensity

gradient (via the Reynolds stress) as well as oscillating pressure-gradient-driven shear [26]; their radial dependence and detailed interaction with the turbulence is presently under investigation. Abbreviated or partial LCO cycles are observed in "regular" L-H transitions, indicating a universal two-stage transition dynamics where transient turbulence-generated shear flow triggers the initial fluctuation suppression in a narrow layer at and just inside the separatrix, and equilibrium shear locks in the transition once the edge pressure gradient has locally increased. Limit cycle oscillations are also observed during the H-L back transition, with evolution dynamics reversed compared to the forward transition. In the initial data shown here, pedestal pressure profile relaxation due to a type-I ELM precedes the LCO back transitions.

References

[1]   Martin Y.R. and Takizuka T. 2008 *J. Phys.: Conf. Ser.* **123** 012033

[2]   Gohil P. *et al* 2011 *Nucl. Fusion* **51** 103020

[3]   McKee G.R. *et al* 2009 *Nucl. Fusion* **49** 115016

[4]   Ryter F. *et al* 2009 *Nucl. Fusion* **49** 062003

[5]   Gohil P. *et al* 2011 *Nucl. Fusion* **50** 064011

[6]   Koide Y. *et al* 1994 *Phys. Rev. Lett.* **72** 3663

[7]   Greenfield C.M. *et al* 2001 *Phys. Rev. Lett.* **86** 4544

[8]   Austin M.E. *et al* 2006 *Phys. Plasmas* **13** 082502

[9]   Waltz R.E. *et al* 2006 *Phys. Plasmas* **13** 075004

[10] Shafer M.W. *et al* 2009 *Phys. Rev. Lett.* **103** 4544

[11] Biglari H., Diamond P.H., Terry P.W. 1990 *Phys. Fluids B* **2** 1

[12] Burrell K.H. 1997 *Phys. Plasmas* **4** 1499

[13] Burrell K.H. *et al* 2004 *Plasma Phys. Control. Fusion* **46** 165

[14] Levinton F. *et al* 1998 *Phys. Rev. Lett.* **80** 4887

[15] McDermott R.M. *et al* 2009 *Phys. Plasmas* **16** 056103

[16] Sauter P. *et al* 2012 *Nucl. Fusion* **52** 012001

[17] Viezzer E. *et al* 2013 *Nucl. Fusion* **53** 053005

[18] Zweben S.J. *et al* 2010 *Phys. Plasmas* **17** 102502

[19] Conway G.D. *et al* 2011 *Phys. Rev. Lett.* **106** 065001

[20] Xu G.S. *et al* 2011 *Phys. Rev. Lett.* **107** 125001

[21] Estrada T. *et al* 2011 *Phys. Rev. Lett.* **107** 245004

[22] Schmitz L. *et al* 2012 *Phys. Rev. Lett.* **108** 155002

[23] Cheng J. *et al* 2013 *Phys. Rev. Lett.* **110** 265002

[24] Shesterikov I. *et al* 2013 *Phys. Rev. Lett.* **111** 055006

[25] Kim E.J. and Diamond P.H. 2003 *Phys. Rev. Lett.* **90** 185006

[26] Miki K. *et al* 2012 *Phys. Plasmas* **19** 092306

[27] Manz P. *et al* 2012 *Phys. Plasmas* **19** 072311

[28] Tynan G.R. *et al* 2013 *Nucl. Fusion* **53** 073053

[29] Hillesheim J.C. *et al* 2009 *Rev. Sci. Instrum.* **80** 083507

[30] Peebles W.A. *et al* 2010 *Rev. Sci. Instrum.* **81** 10D902

[31] Hirsch M. *et al* 2001 *Plasma Phys. Control. Fusion* **43** 1641

[32] Smirnov A.P. and Harvey R.W. 2001 The GENRAY ray tracing code, *CompX Report COMPX-2000-01*.

[33] Hillesheim J.C. *et al*. 2010 *Rev. Sci. Instrum.* **81** 10D907

[34] Kobayashi T. *et al* 2013 *Phys. Rev. Lett.* **111** 035002

[35] Miki K. *et al* 2013 *Nucl. Fusion* **53** 073044

List of Figure Captions

Figure 1. (Color online) (a) Divertor D_α emission, (b) density fluctuation level at $R = 2.25$ m; (c) electron temperature at $R = 2.23$ m, and line-averaged plasma density; (d) frequency spectrum of $E \times B$ flow velocity, and (e) rms level of $E \times B$ flow (at $R = 2.25$ m), and (f) neutral beam power, during an L-LCO-H transition with extended limit cycle oscillations.

Figure 2. (Color online) (a) $E \times B$ velocity, (b) normalized density fluctuation level $\tilde{n}/n$, and (c) D_α signal. (d) Limit cycle between density fluctuation level and $v_{E \times B}$ during the LCO; the start of the LCO (t_0) and the final transition to H-mode (t_H) are indicated; (e) partial limit cycle during a "regular" L-H transition; 4.5 cm inside the LCFS (orange), and 3.5 cm inside the LCFS (red).

Figure 3. (Color online) (a) Flow velocity across the L-LCO-H transition, measured by DBS at the separatrix (upper trace $R = 2.27$ m), near the center of the electric field well (middle trace $R = 2.25$ m, and inboard of the electric field minimum (lower trace $R = 2.225$ m); the error in velocity is estimated as ± 0.5 km/s; (b) corresponding normalized density fluctuation levels at $R = 2.27$ and 2.25 m; (c) at $R = 2.225$ m; the error in $\tilde{n}/n$ is estimated as ± 0.04 (au).

Figure 4. (Color online) Radial profile of normalized density fluctuation level in (a) L-mode; (d) H-mode; radial density profile from profile reflectometry in (b) L-mode; (e) H-mode; radial profile of $E \times B$ velocity in (c) L-mode; (f) H-mode. Data from ± 2 ms around the L-mode and H-mode reference times (1264 ms, 1290 ms) are included.

Figure 5. (Color online) Auto-correlation coefficient (black) of the reference channel and radial cross-correlation coefficients between the reference channel and 2–3 probing radii displaced radially by 0.25 cm (red), 0.5 cm (green), and 0.75 cm (blue), respectively. The derived radial correlation length of density fluctuations during the LCO (a,b) and during ELM-free H-mode (c) is indicated.

Figure 6. (Color online) (a) Density fluctuation level 0.5 cm inside the LCFS; (b) decorrelation rate (dotted line) and shearing rate (solid line) 0.5 cm inside the LCFS, (c) density fluctuation level 2 cm inside the LCFS; (d) decorrelation rate (dotted line) and shearing rate (solid line) 2 cm inside the LCFS, (e) density gradient spanning the two radii (0.5 cm and 2 cm inside the LCFS); (f) main ion diamagnetic velocity spanning the same radii and (g) D_α signal.

Figure 7. (Color online) Cross-correlation coefficient between the $E \times B$ shearing rate and the density fluctuation level, (a) for different times with respect to the start time t_0 of the LCO, (b) in the "regular" transition during the abbreviated limit cycle (1294.63 ms) and at 1296.03 ms just before the final D_α drop (indicating completion of H-mode transition).

Figure 8. (Color online) (a) D_α recycling light, (b) $\tilde{n}$, (c) ZF (LCO) frequency, (d) magnitude of $E \times B$ velocity, and (e) neutral beam power during H-L and L-H transitions with LCO.

Figure 9. (Color online) Time evolution of (a) $E \times B$ velocity, (b) shearing rate at $r/a = 0.5$ during electron ITB formation, and (c) normalized density fluctuation amplitude near the $q = 2$ surface.

Figure 10. (Color online) (a) Radial electron temperature profile at 1205–1285 ms, showing electron ITB formation at $r/a \sim 0.5$, and (b) ion temperature profile showing ion ITB at 1271 ms.

Figure 11. (Color online) Radial profiles of (a) electron temperature, (b) inverse temperature gradient scale length, (c) $E \times B$ velocity, and (d) normalized density fluctuation level $(k_\theta \rho_s \sim 2)$, across the electron transport barrier.

Figure 12. (Color online) Time series of density fluctuation amplitude $($upper trace, $k_\theta \rho_s \sim 2)$ and the instantaneous $E \times B$ shearing rate $\omega_{E \times B}$ (lower trace); $r/a \sim 0.47$.

Figure 13. (Color online) Cross correlation coefficient between rms density fluctuation level and $E \times B$ flow shearing rate; velocity indices correspond to measurement locations shown in figure 11(c): (a) ch 1–2, r/a~0.47; (b) ch 2–3, r/a~0.48; (c) ch 3–4, r/a~0.49.
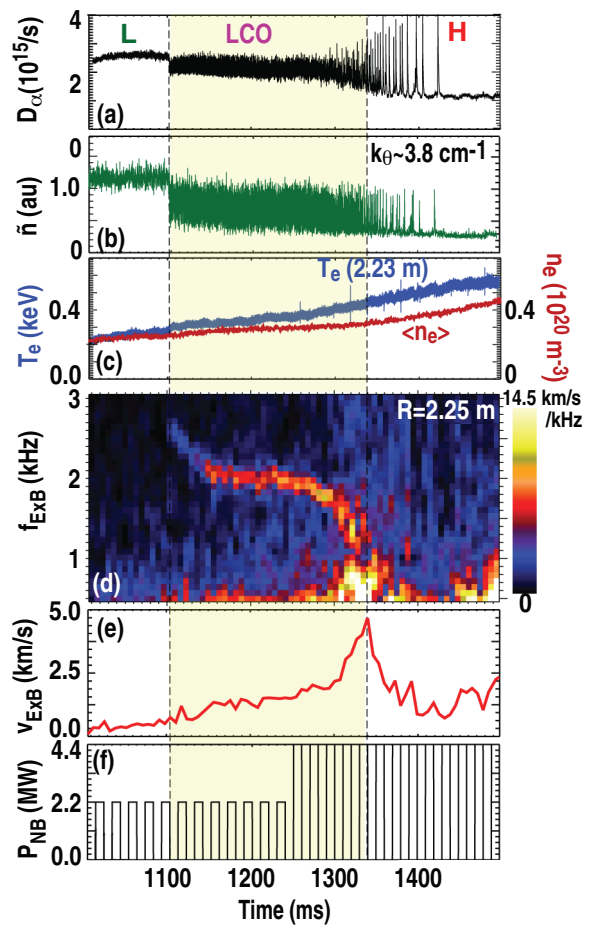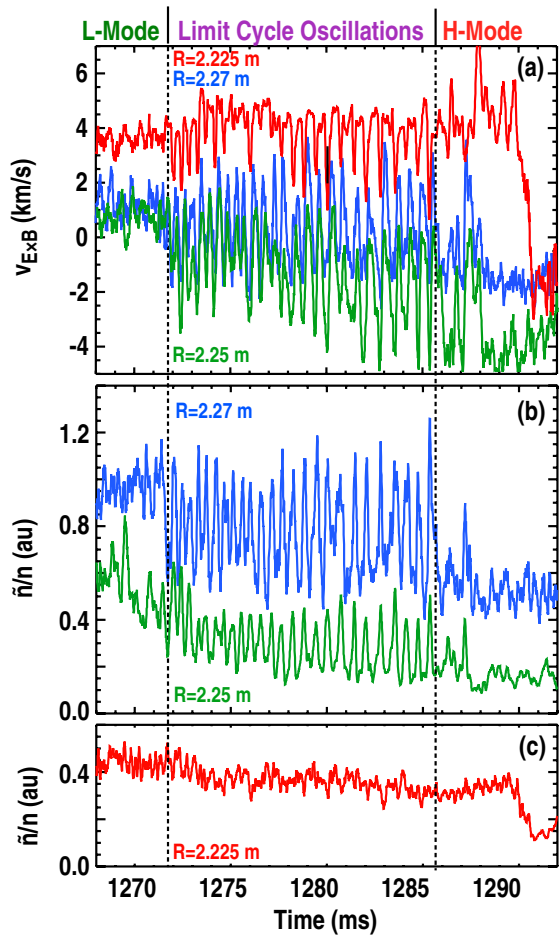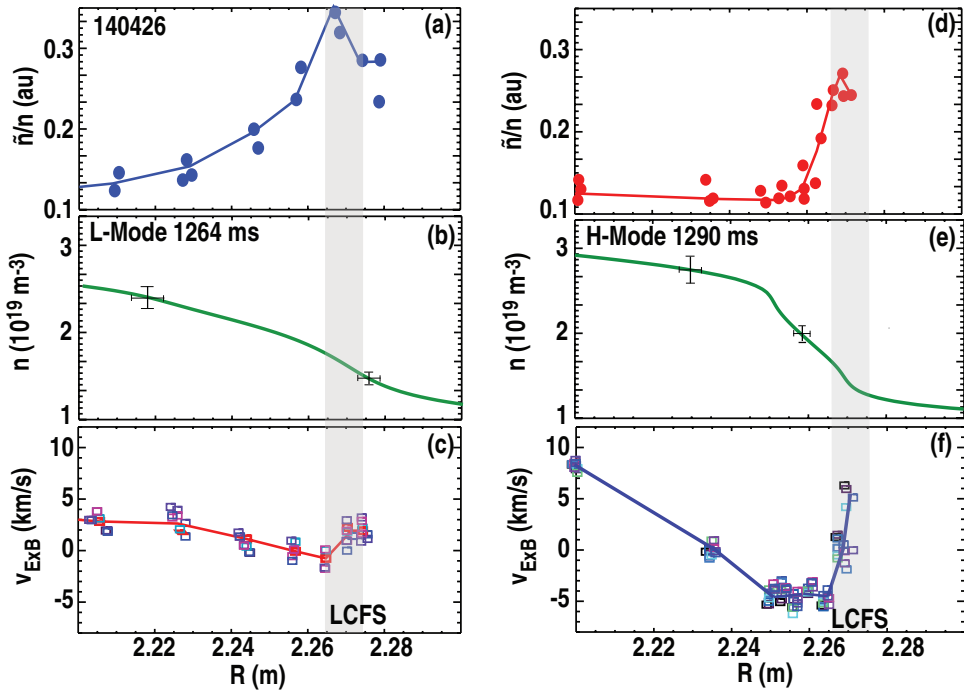
L. Schmitz   Figure 1
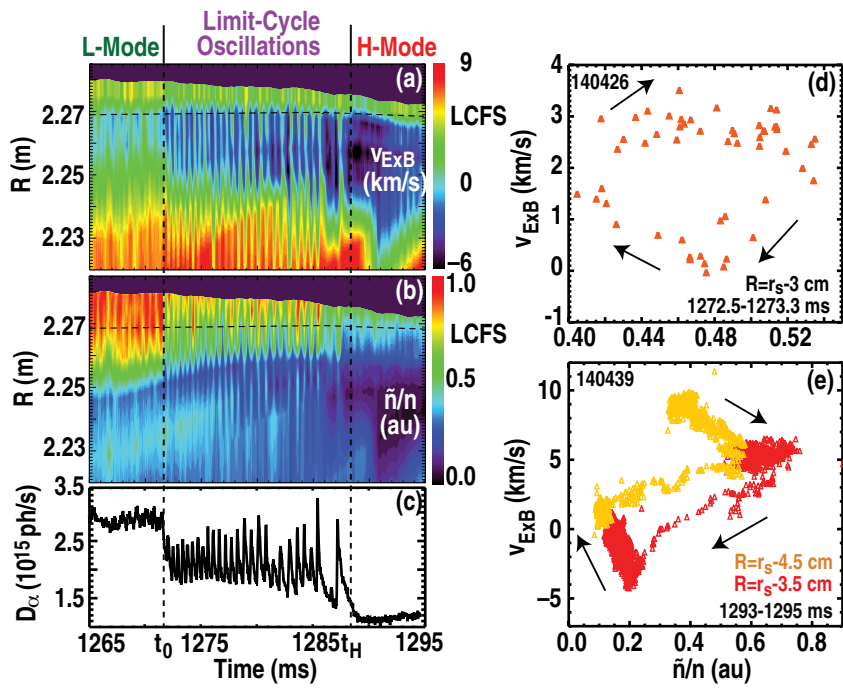
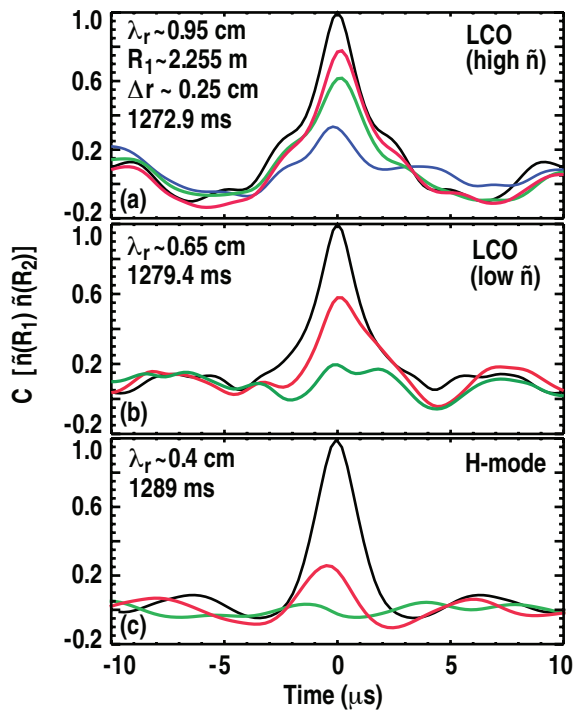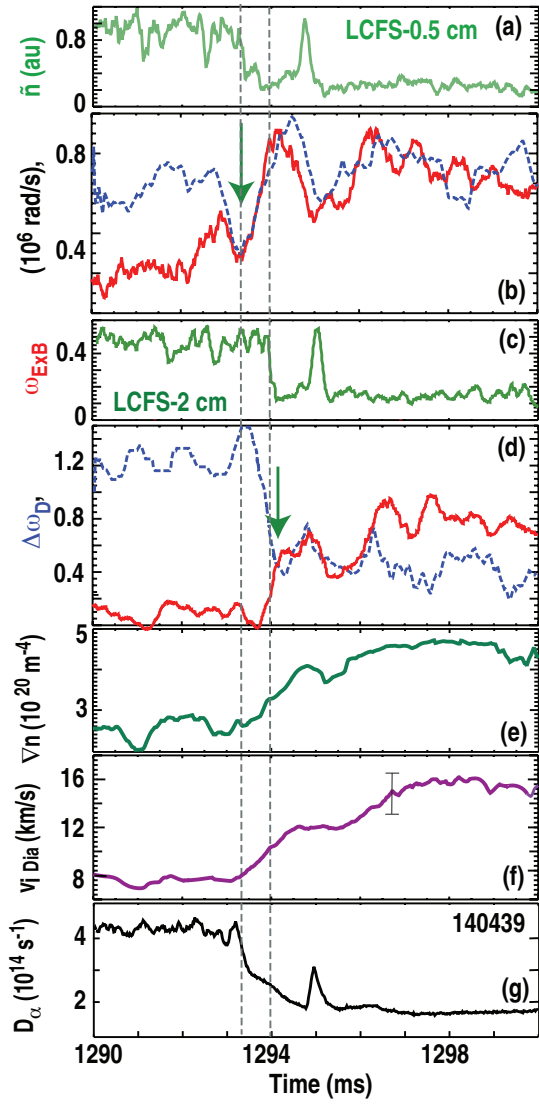L. Schmitz   Figure 2
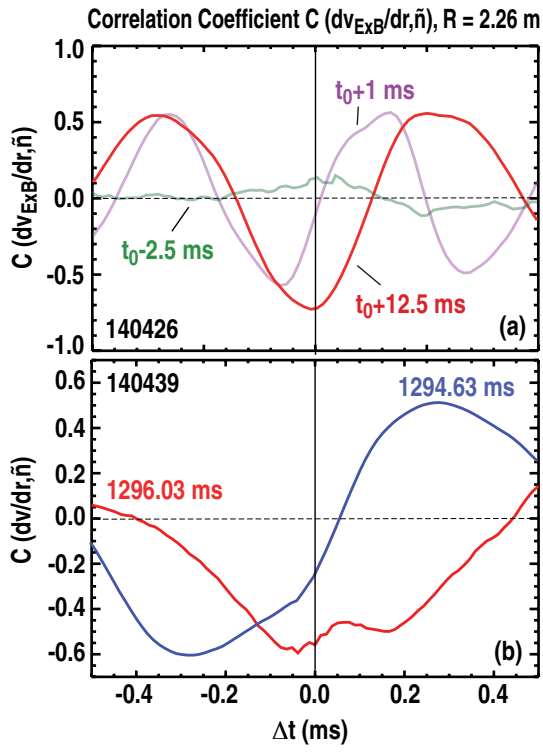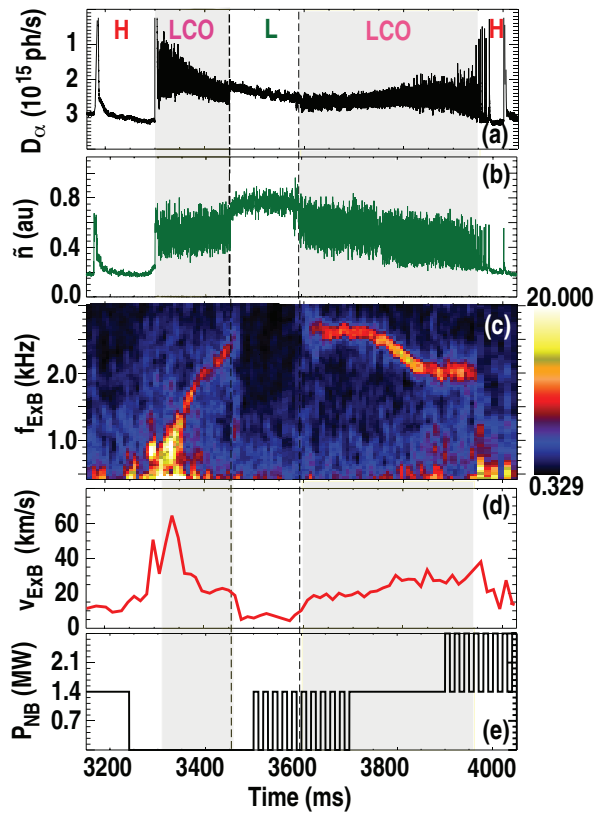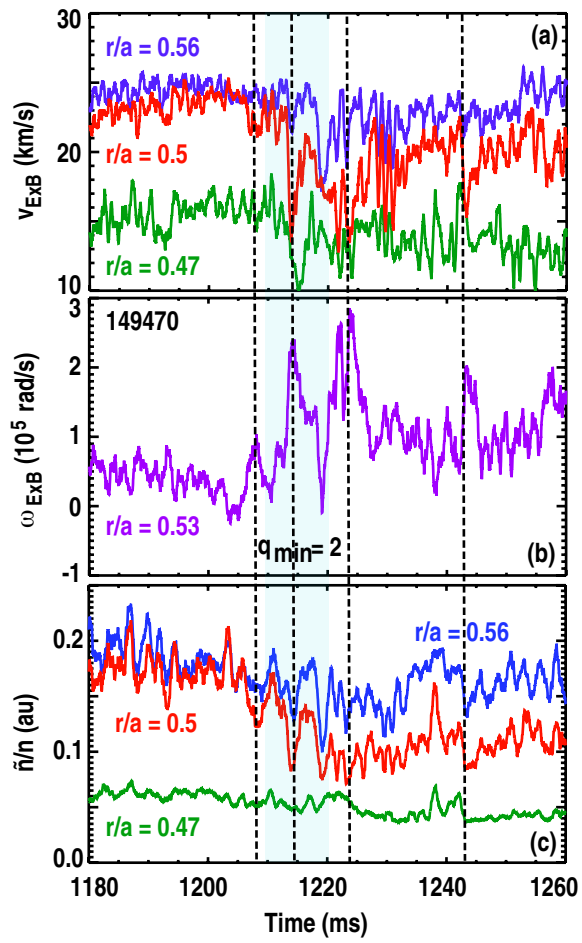
L. Schmitz   Figure 3

140426

L-Mode 1264 ms

H-Mode 1290 ms

LCFS

LCFS

L. Schmitz   Figure 4

L. Schmitz   Figure 5

(a) ñ (au), LCFS-0.5 cm

(b) ω$_{ExB}$ (10^6 rad/s),

(c) LCFS-2 cm

(d) Δω$_D$,

(e) ∇n (10^{20} m^{-4})

(f) v$_{i Dia}$ (km/s)

(g) D$_α$ (10^{14} s^{-1}), 140439

Time (ms)

L. Schmitz   Figure 6

Correlation Coefficient C $(dv_{ExB}/dr, \tilde{n})$, R = 2.26 m

(a) 140426

t_0+1 ms

$t_0-2.5$ ms

$t_0+12.5$ ms

(b) 140439

1294.63 ms

1296.03 ms

Δt (ms)

L. Schmitz   Figure 7
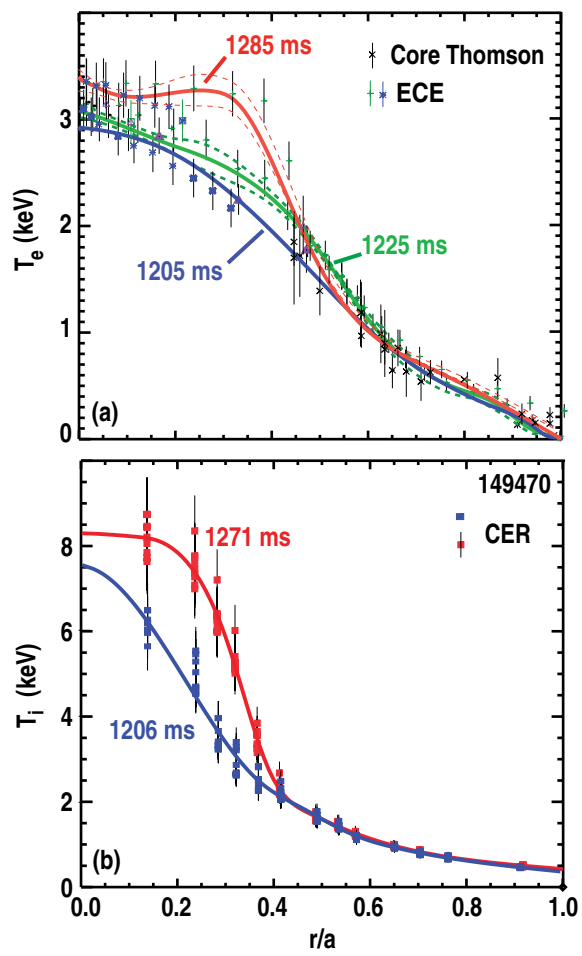
L. Schmitz   Figure 8
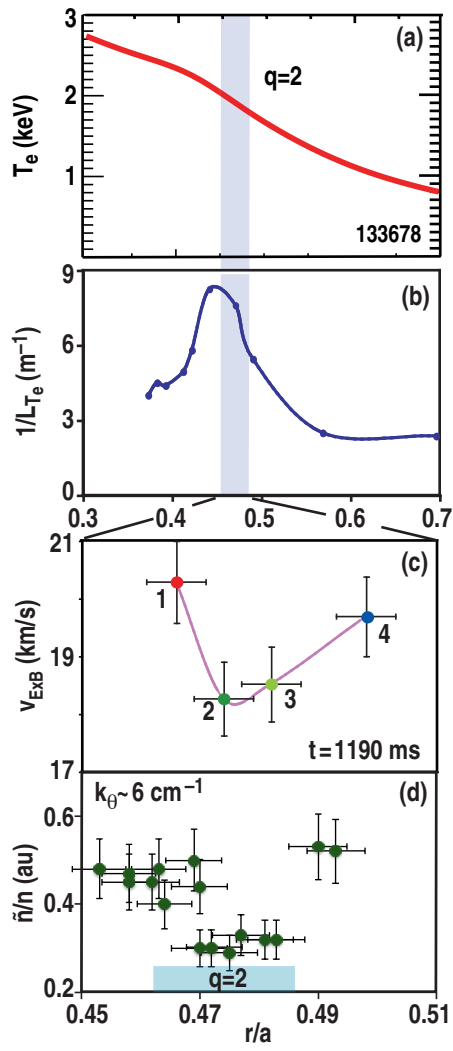
L. Schmitz   Figure 9

(a)

T_e (keV)

1285 ms

× Core Thomson

ECE

1225 ms

1205 ms

(b)

149470

T_i (keV)

1271 ms

CER

1206 ms

r/a

L. Schmitz   Figure 10

(a) q=2

133678

T_e (keV)

(b)

$1/L_{T_e}$ (m^{-1})

(c)

v_{ExB} (km/s)

t = 1190 ms

(d)

$k_\theta \sim 6$ cm^{-1}

$\tilde{n}/n$ (au)

q=2

r/a

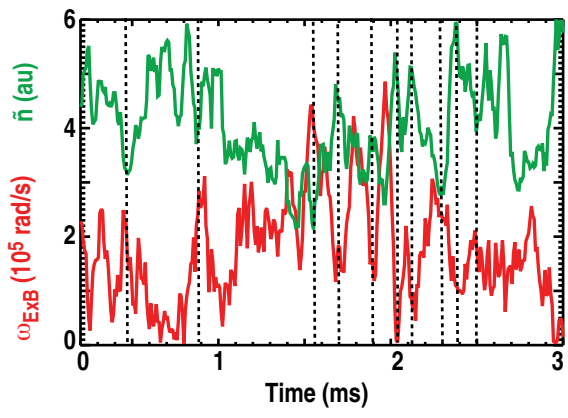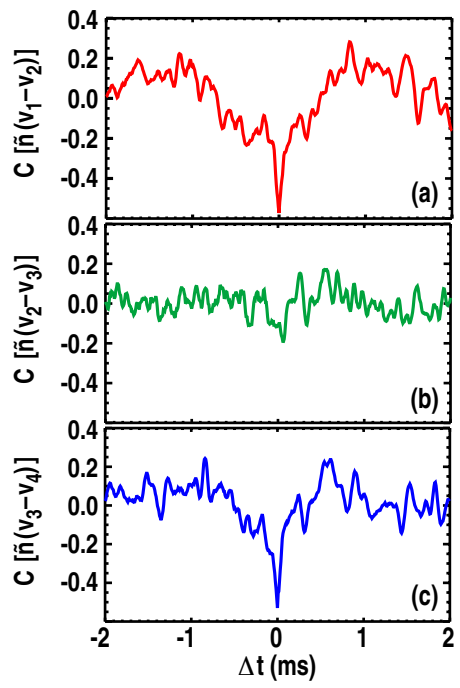L. Schmitz   Figure 11

L. Schmitz   Figure 12

L. Schmitz   Figure 13